Biosensors and Bioelectronics 288 (2025) 117754

Contents lists available at ScienceDirect

Biosensors and Bioelectronics

journal homepage: www.elsevier.com/locate/bios

Resolving SPARC–HSA binding kinetics with an ultrasensitive photonic sensor based on bound states in the continuum

Bruno Miranda [a,*,1], Vincenza Mele [b,1], Aida Seifalinezhad [a,c], Gianluigi Zito [a], Adam Schwartzberg [d], Vito Mocella [a], Ivo Rendina [a], Annalisa Lamberti [b], Gennaro Sanità [a,*], Silvia Romano [a]

[a] Institute of Applied Sciences and Intelligent Systems, National Research Council, Via Pietro Castellino 111, Naples, 80131, Italy
[b] Department of Molecular Medicine and Medical Biotechnology, University of Naples Federico II, Via Pansini 5, Naples, 80131, Italy
[c] Department of Engineering, Università degli Studi di Napoli Parthenope, Centro Direzionale di Napoli, Isola C4, Naples, 80143, Italy
[d] Molecular Foundry, Lawrence Berkeley National Laboratory, 1 Cyclotron Road, Berkeley, 94720, CA, USA

ARTICLE INFO

Keywords:
Photonic crystals
Bound states in the continuum
SPARC
Albumin
Dissociation constant

ABSTRACT

Secreted protein acidic and rich in cysteine (SPARC) is critical in cell–matrix interactions and tissue remodeling. It influences tumor progression through its affinity for human serum albumin (HSA) - the most abundant plasma protein, which also plays a crucial role in drug delivery. Strong molecular binding leads to a dissociation constant K_D in the nanomolar range. Thus, determining K_D requires detecting sub-nanomolar concentrations with ultrasensitive methods. This may be crucial for elucidating the nature of SPARC–HSA binding, as their interaction remains a subject of debate. Capturing these interactions accurately requires a platform capable of resolving rapid binding kinetics at extremely low analyte concentrations. In this work, we report on a microfluidics-integrated photonic nanostructure that supports bound states in the continuum (BICs) and is optimized for studying the fast kinetics of high-affinity protein–protein interactions. The unprecedented capability of detecting sub-nanomolar concentrations allows quantifying K_D between SPARC and HSA beyond the state of the art. We leverage an all-dielectric photonic crystal slab (PhCS) sustaining two BIC branches arising from gapped Dirac cone dispersion. HSA is covalently immobilized on the PhCS bonded to a PDMS microfluidic chamber. SPARC dissociation is carried out using PBS buffer (pH 7.4), ensuring complete protein release through precise control of the flow rate and continuous spectral monitoring of the BICs. The measured $K_D = 8.2 \pm 0.8$ nM confirms the strong affinity of SPARC for HSA. This study highlights the potential of BIC-based sensing as a versatile tool for investigating protein interactions. These results also have implications for the optimization of drug delivery systems and cancer treatment strategies.

1. Introduction

Secreted protein acidic and rich in cysteine (SPARC), also known as osteonectin, is a matricellular protein involved in a wide range of cellular processes, including extracellular matrix (ECM) regulation, cell proliferation, and stress response (Tai and Tang, 2008). It is widely expressed in remodeling tissues, including bone, skin, and cancerous environments, and plays a critical role in the regulation of cell-ECM interactions, growth factor activity, and angiogenesis (Johnson and Smith, 2002; Liu and Zeng, 2014). Numerous studies have shown a strong correlation between SPARC expression levels and the progression and severity of various solid tumors, including pancreatic carcinoma, melanoma, and breast carcinoma (Andriani et al., 2018; Ghanemi et al., 2020).

Protein–protein interactions play a key role in the regulation of the biological processes involved in tissue physiology and pathology. Among these, the interaction between SPARC and human serum albumin (HSA) has gained increasing attention due to its potential role in the design of albumin-bound drugs, such as nab-paclitaxel, which are administered preferentially to tumors expressing SPARC (Vishnu and Roy, 2011; Carrese et al., 2021, 2023). Their selective binding affinity provides the possibility to understand how tumor cells exploit metabolic pathways and resource distribution, since albumin serves as a critical reservoir for nutrients and signaling molecules (Zhao et al., 2018; Belinskaia et al., 2021).

* Corresponding authors.
E-mail addresses: bruno.miranda@cnr.it (B. Miranda), gennaro.sanita@na.isasi.cnr.it (G. Sanità).
[1] Shared Authorship.

https://doi.org/10.1016/j.bios.2025.117754
Received 28 February 2025; Received in revised form 13 June 2025; Accepted 2 July 2025
Available online 16 July 2025

The determination of kinetic parameters, such as the dissociation constant K_D of the SPARC-HSA complex, is crucial for the stability and affinity of this interaction under physiological and pathological conditions and for the prediction of the behavior of albumin drugs in cancer disease (Chlenski et al., 2016). The K_D provides information on the dynamics of complex formation and dissociation, thus offering predictive value for its functional behavior *in vivo*. Indeed, it can refine drug delivery systems and translational medicine, improving therapeutic efficacy and minimizing off-target effects (Carrese et al., 2021; Ji et al., 2024). Monitoring association and dissociation kinetics provides a more detailed understanding of molecular interactions compared to measuring the steady state K_D (equilibrium dissociation constant) alone (Aarons, 1981; Giannetti et al., 2008). This approach offers several advantages. First, it provides comprehensive binding information, since the kinetics, including the association rate k_a and the dissociation rate k_d, give a dynamic picture of the speed with which molecules associate and dissociate, revealing the binding strength based on fast association, slow dissociation, or both. Second, it allows the distinction of different mechanisms of binding. For example, two interactions might have similar K_D values, while their kinetic profiles could differ significantly: one interaction might exhibit rapid binding and dissociation, yet another binds slowly but dissociates very slowly. This distinction is crucial for understanding biological functions or designing drugs. Moreover, monitoring kinetics is highly relevant under *in vivo* conditions, where interactions rarely reach equilibrium (Giannetti et al., 2008). Instead, this approach better mimics transient interactions, especially in systems with competing interactions or changing conditions, such as those found in cellular environments. In drug development, detailed kinetic profiles are instrumental in optimizing drug candidates for specific therapeutic goals, such as fast-acting or long-lasting effects. Lastly, analysis of kinetics can identify off-rate dominance. If the dissociation rate (k_d) is the primary determinant of K_D, targeting k_d — for example, by reducing dissociation — can be a strategic approach to improve the binding affinity (Copeland, 2016).

Since strong molecular binding leads to a dissociation constant K_D in the nanomolar range, accurately determining K_D requires resolving the kinetics of sub-nanomolar concentrations of analytes through ultrasensitive methods. Although crucial for devising new strategies based on SPARC-HSA interactions, there are inconsistent attributions to the binding affinity between SPARC and HSA, and this lack of robust quantification is likely due to poor detection sensitivity.

Photonic bound states in the continuum (BICs) are discrete eigenmodes embedded in the continuum of radiating waves (Bulgakov and Sadreev, 2008; Plotnik et al., 2011; Molina et al., 2012; Hsu et al., 2013b; Zhen et al., 2014; Bulgakov and Sadreev, 2014; Mocella and Romano, 2015; Gomis-Bresco et al., 2017). First introduced in the context of quantum mechanics (von Neumann and Wigner, 1929), BICS have since been identified across a wide range of photonic systems, including metasurfaces, plasmonic structures, photonic crystals and fiber Bragg gratings (Gansch et al., 2016; Bulgakov and Maksimov, 2018; Kupriianov et al., 2019; Gao et al., 2019). These states emerge from several distinct mechanisms, such as symmetry mismatch (Plotnik et al., 2011), fine-tuned parameters (Hsu et al., 2013a), and inverse design strategies (Ma et al., 2022; Chen et al., 2024). In contrast to other leaky optical modes, BICs do not couple to radiative modes and are therefore characterized by an ideally infinite radiative Q-factor owing to nontrivial topological properties (Zito et al., 2019; Wang et al., 2020; Cerjan et al., 2020; De Tommasi et al., 2021, 2023; Schiattarella et al., 2024). Thanks to these unique features, BICs have demonstrated significant advantages and potential applications in manipulating light fields and modulating light–matter interactions. Notably, they have been successfully employed in the development of lasers (Hwang et al., 2021; Yu et al., 2021; Do et al., 2025) and filters (Foley et al., 2014; Lu et al., 2024). Moreover, dielectric nanostructures sustaining BICs have emerged as highly sensitive sensors for label-free, real-time and imaging measurement (Liu et al., 2017; Romano et al., 2018b,a, 2019; Yesilkoy et al., 2019; Romano et al., 2020; Maksimov et al., 2020; Zito et al., 2021; Schiattarella et al., 2022; Zito et al., 2024; Clabassi et al., 2025).

In this work, we demonstrate a microfluidics-integrated photonic crystal slab (PhCS) especially engineered for studying the fast kinetics of high-affinity protein–protein interactions by leveraging BIC-based refractometric sensing. The capability of this system to detect sub-nanomolar concentration ranges enables quantification of K_D between SPARC and HSA, beyond the state-of-the-art. By leveraging the ultra-high Q-factor of BICs, the system demonstrates sufficient sensitivity to refractive index changes induced by molecular binding events for resolving fast-kinetics processes. This approach ensures a precise determination of the dissociation constant (K_D), providing crucial insights into SPARC-HSA interaction dynamics. In particular, we found an association rate constant $k_a = (1.7 \pm 0.2) \times 10^6\ \mathrm{M^{-1}s^{-1}}$ and a dissociation rate constant $k_d = (1.4 \pm 0.1) \times 10^{-2}\ \mathrm{s^{-1}}$, leading to a dissociation constant $K_D = 8.2 \pm 0.8$ nM and confirming the high affinity of the interaction between SPARC and HSA proteins. The proposed BIC biosensor offers significant advantages over traditional techniques, such as surface plasmon resonance (SPR) and enzyme-linked immunosorbent assays (ELISA), including higher sensitivity and lower heat losses. Moreover, it features a compact and scalable design for its integration into portable diagnostic devices. In principle, enabling point-of-care applications in cancer diagnostics and therapeutic monitoring.

2. Experimental section

2.1. Design and simulation

Numerical simulations of the transmittance spectra of the PhCSs as a function of the incident angle were conducted using a comprehensive, three-dimensional, rigorous coupled-wave approach (RCWA) based on a Fourier modal expansion. Ansys Lumerical 2023 was employed for these simulations. Bloch periodic boundary conditions were applied along the x- and y-directions (unit cell lateral directions). The refractive index of the substrate was set as 1.46, corresponding to quartz. The refractive index of the surrounding medium (top cladding) was set as 1 for air and 1.33 for the aqueous environment. The silicon nitride (Si_3N_4) dispersion was obtained by spectroscopic ellipsometry.

2.2. Fabrication and optical characterization

The PhCS sensor with an area of 1 mm^2 consists of a square lattice of cylindrical holes in silicon nitride (Si_3N_4) deposited on a SiO_2 substrate through plasma-enhanced chemical vapor deposition (PECVD) (Romano et al., 2020). The design was patterned using standard high-voltage electron beam lithography (Zito et al., 2021; Schiattarella et al., 2022). The PhCS samples were optically characterized using a dedicated optical setup. The spectral position and the origin of different types of modes were investigated via angle-resolved transmission spectroscopy using a collimated supercontinuum laser (NKT Photonics, SuperK EXTREME). A computer-controlled rotational stage allowed angle-resolved measurements with a resolution of 0.01° (Romano et al., 2014). Transmission spectra were acquired by using an Ocean Optics USB4000 spectrometer with a resolution of 0.25 nm for different incident angles θ of the incoming beam. The band diagrams were reconstructed via a custom-built MathWorks MATLAB routine for acquisition and band reconstruction, including a filtering process via fast Fourier transform to remove the background noise.

2.3. Surface functionalization and optofluidic chip assembly

The surface functionalization of Si_3N_4 PhCSs was performed by following a well-established protocol for silicon-based substrates. PhCSs were cleaned through three washes with absolute ethanol, followed by three washes with double-distilled water (ddH_2O) for 5 min at room temperature (RT). To introduce silanol groups (Si-OH) on the silicon nitride surface, the crystals were immersed in hexane (5 min at RT), in ddH_2O (5 min at RT), and Piranha solution (H_2SO_4:H_2O_2 3:1 v/v) for 30 min at 90 °C. Then, sequential immersions in aqueous solutions of NaOH 0.5 M and HCl 0.1 M were performed. Finally, the PhCSs were washed with (ddH_2O) (5 min at RT). To introduce amino groups (–NH_2) through silanization, the surfaces were immersed in APTES (3-aminopropyl-triethoxysilane) solution (5% v/v in anhydrous toluene) for 120 min at 37 °C. Next, the crystals were washed three times with toluene (2 min at RT) and heated at 100 °C for 10 min (curing), followed by functionalizion with BS^3 (bis(sulfosuccinimidyl)suberate) at 10 mM in 20 mM HEPES buffer pH 7.5 for 5 h at 4 °C. After three washes with 20 mM HEPES buffer pH 7.5 and with (ddH_2O) (5 min at RT), PhCSs were incubated with SPARC (14 μM, 5 μL) or rHSA (7 μM, 5 μL) in PBS 1x at 4 °C overnight. Before incubation with rHSA or SPARC, the N-hydroxysuccinimide ester (NHS) groups of BS^3 molecules that had not reacted with SPARC or rHSA were saturated with a solution of Tris–HCl 200 mM, pH 7.5 for 30 min at RT. Finally, the PhCSs were washed three times with PBS 1x for 5 min at RT.

After each functionalization step, band diagrams were acquired as described in the previous section, and the possibility of monitoring the interaction of the bioprobe with its target under static conditions was assessed by allowing association in PBS for 30 min at room temperature and dissociation in HEPES buffer for 50 min.

The dissociation constant between SPARC and HSA was finally determined using the optimized functionalization strategy under dynamic conditions, which involved integrating a microfluidic chamber into the functionalized PhCS. The microfluidic chamber was made using a soft lithography technique PDMS (polydimethylsiloxane) starting from a 10:1 w/w prepolymer solution of PDMS mixture, poured into a Petri dish, degassed in a vacuum chamber to remove air bubbles, and cured for 3.5 h at 60 °C. The microfluidic chip is composed of an incubation chamber, an inlet, and an outlet, interconnected by a 0.5 mm thin channel. The incubation chamber is nothing but a cylindrical hole with a radius of 1.5 mm. The whole height of the microfluidic chip is 0.2 mm. Two holes were punched inside the chamber to allow inflow and outflow of the solution. Two bent needles connected the syringe tubes to the channel, allowing the solution to flow. Finally, the chamber was bonded to the PhCS surface at the bottom through an oxygen plasma process and thermal curing at 50 °C for 5 min. The liquid flow was controlled using a syringe infusion pump (KD Scientific), which allowed the total infusion volume to be monitored. Association and dissociation experiments were carried out for 30 min each at a constant flow rate of 10 μL/min in PBS. During association phases, several concentrations of SPARC were tested (0.25, 0.5, 1, 2, 4, 8, 16 nM), while during dissociation, the syringe fluid was substituted with PBS to restore equilibrium and remove all the bound molecules. A blank measurement (SPARC concentration = 0 nM) was also performed by incubating PBS for 30 min at a constant flow rate of 10 μL/min. Each experiment was repeated at least in triplicate ($n \geq 3$).

2.4. Materials and reagents

Ethanol was purchased from VWR BDH chemicals. Hexane, anhydrous toluene, bis(sulfosuccinimidyl)suberate (BS^3), 3-aminopropyl-triethoxysilane (APTES), and recombinant human serum albumin (HSA) were purchased from Sigma-Aldrich Chemical Company Inc. Phosphate-buffered saline (PBS) was purchased from Gibco. Sodium hydroxide and Hydrochloric acid 37% were purchased from Carlo Erba Reagents. Tris and HEPES were purchased from ITW Reagents. Human SPARC Recombinant Protein was purchased from Thermo Fisher Scientific Inc. Ultrapure water was obtained from a Millipore water purification system (18.2 MΩ cm^{-1}, Milli-Q, Millipore). Polydimethylsiloxane (PDMS) and its curing agent were obtained from Dow Corning, Germany.

3. Results and discussion

The study of protein-protein interactions is of paramount importance in the biomedical field for the optimization of drug delivery systems and cancer treatment strategies. To this aim, the combination of photonic nanostructures with microfluidics represents a powerful strategy. We combined a PhCS sustaining BIC with a microfluidic system to enable the continuous monitoring of the association and dissociation of SPARC protein on HSA-functionalized PhCS. First, a thorough numerical analysis was carried out to predict the PhC performance. Then, the functionalization strategy and operating conditions were optimized. Finally, association and dissociation kinetics were investigated.

3.1. Optimization of the PhCS geometry

Fig. 1a shows a schematic representation of the proposed device consisting of a silicon nitride PhCS on a quartz slide and enclosed in a microfluidic chamber in PDMS (optically transparent in the visible range). The geometric design followed a specific strategy. Three parameters were considered for the simulations: the hole radius r, the slab thickness t, and the lattice constant a (Fig. 1b), finely tuned to predict the experimental transmittance band diagram. By monitoring the peak wavelengths of the three principal modes, indicated as λ_1, λ_2, and λ_3, as a function of r, t, and a, it was possible to investigate the emergence of two BIC modes at Γ point. These correspond to λ_2 and λ_3 as their linewidth progressively vanishes for incidence angles approaching normal incidence (Γ), which can be associated with the characteristic diverging Q-factor of BICs (Fig. 1c).

For sufficiently large r and small t (*i.e.*, $r > 107$ nm when $a = 363$ nm and $t = 56$ nm or $t < 48$ nm, when $a = 363$ nm and $r = 86$ nm), the modes are degenerate at the Γ point in momentum space, supporting the formation of a Dirac cone (Romano et al., 2020; Zito et al., 2024). The evolution of the modes as a function of r and t (Fig. 1c) shows that the Dirac cone is gapped below certain values of r and above certain values of t, with the emergence of two BICs. At the same time, it is possible to tune their spectral position at λ_2 and λ_3, by changing the lattice constant a. The spectral separation among the three modes can be tuned by adjusting the r/t ratio, regardless of a. In Fig. 1d, representative band diagrams are reported as a function of the geometrical parameters, which provides a better understanding of the evolution of the dispersion curves (see also Figures S1-S3 from supporting information). It should be noted that the increase in t, at fixed a and r, significantly affects the linewidth of λ_1 and λ_3.

Numerical simulations were carried out to achieve the exact positioning of the selected resonances and to study their evolution as a function of the functionalization layers, as shown in the next section. Fig. 1e shows the predicted and measured transmittance spectra (s-polarization, TE-like modes). As shown, excellent agreement between theory and experiments is achieved ($r = 95$ nm, $t = 56$ nm, $a = 363$ nm). The narrow linewidth of mode λ_2 was experimentally resolved only after incubation in the buffer solution, owing to the Q-factor decrease caused by surface radiative losses, in agreement with a previous report (Zito et al., 2024).

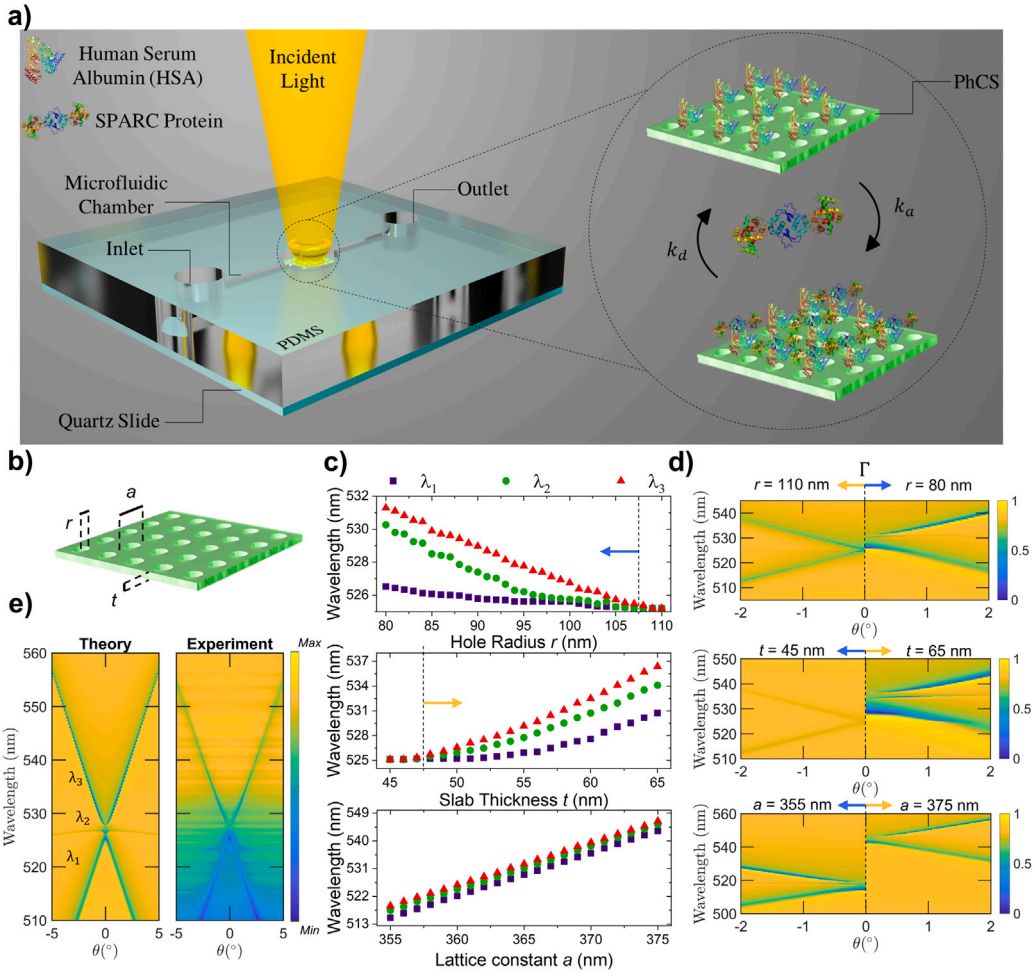

Fig. 1. (a) Schematic representation of the microfluidic-integrated optical device for the accurate determination of SPARC/HSA dissociation constant. (b) PhCS sketch showing a Si_3N_4 slab having thickness t, and patterned with a square lattice (lattice constant a) of holes with radius r. (c) Parametric tuning of the PhCS modes position λ_1, λ_2, and λ_3 as a function of r, t, and a in the Γ point ($\theta = 0°$). The arrows denote Dirac cone splitting as a function of the decreasing r and increasing t. (d) Comparison of the simulated band diagrams for TE-like modes (s-polarization) as a function of the incidence angle θ obtained as a function of r (r = 110 nm, on the left, and r = 80 nm, on the right), t (t = 45 nm, on the left, and t = 65 nm, on the right), and a (a = 355 nm, on the left, and a = 375 nm, on the right). (e) Simulated transmittance band diagrams (r = 95 nm, t = 56 nm, and a = 363 nm) compared with experimental band diagram of the PhCS for TE-like modes (s-polarization) as a function of the incidence angle θ.

3.2. Numerical investigation of the PhCS sensing performance

Numerical simulations were carried out to predict the refractometric sensitivity of the two modes λ_2 and λ_3 as a function of both refractive index n and thickness δt of the superficial layer. Furthermore, two environment claddings were considered to achieve a more accurate representation of the sensor capability to detect SPARC/HSA interaction: a cladding refractive index $n_{cladding}$ = 1.0 (measurements after sample drying); and $n_{cladding}$ = 1.33, mimicking measurements carried out in PBS buffer under continuous spectral monitoring.

Fig. 2a reports the transmittance band diagrams (s-pol) obtained for r = 95 nm, t = 56 nm, and a = 363 nm with $n_{cladding}$ = 1.0, considering a thin layer with a refractive index of 1.42 with increasing thicknesses $\delta t = 0, 4$, and 7 nm. The value δt was chosen in agreement with the hydrodynamic radii of SPARC and HSA, which are 4, and 7 nm, respectively. The refractive index of the layer was chosen to approximate the immobilization of the two biomolecules on the PhCS surface (Guo et al., 2024). Both modes, λ_2 and λ_3, undergo a redshift as a function of δt for all incident angles θ, as shown in the Supporting Information (Figure S4). The redshift of λ_3 tends to decrease with the incident angle θ.

The shift of the peak wavelength, $\Delta\lambda$, for both BIC modes was evaluated at fixed incidence angle (3°) by varying the biolayer refractive index and thickness, considering an environment cladding of air (Fig. 2b–c). Both $\Delta\lambda_2$ and $\Delta\lambda_3$ increased exponentially with the refractive index when the biolayer was 7-nm thick. In contrast, when δt = 4 nm, mode λ_2 followed a nearly linear trend, and only mode λ_3 retained its exponential behavior. At a fixed film refractive index (n=1.42), $\Delta\lambda_2$ = 0.9 nm and 1.5 nm for δt = 4, and 7 nm, respectively, whereas $\Delta\lambda_3$ = 0.3 nm and 0.7 nm for δt = 4 and 7 nm, respectively. The different behavior of mode λ_2 in air as a function of the different layer thicknesses led us to consider only mode λ_3 for the monitoring of the functionalization steps, thus evaluating all spectral shifts with a consistent approach.

Fig. 2(d) illustrates the transmittance band diagrams (s-pol) obtained from the same PhCS for $n_{cladding}$ = 1.33. Also in this case, both modes λ_2 and λ_3 undergo a redshift as a function of δt. However, the redshift of λ_3 remains nearly unvaried for increasing incident angle θ (see also Figure S5 from the Supporting Information).

The two BIC branches exhibit an even higher sensitivity to the refractive index variation (Fig. 2e–f). Both $\Delta\lambda_2$ and $\Delta\lambda_3$ were larger in a lower range (1.33–1.60). This suggests increased surface sensitivity when operated in wet conditions, consistently with the larger penetration depth of the evanescent field, which is more advantageous for continuous monitoring applications. Both modes follow a linear trend in this refractive index range, and their sensitivity increases as a function of δt, as expected. Also in this case, we selected mode λ_3 for real-time experiments for consistency with the previous choice.

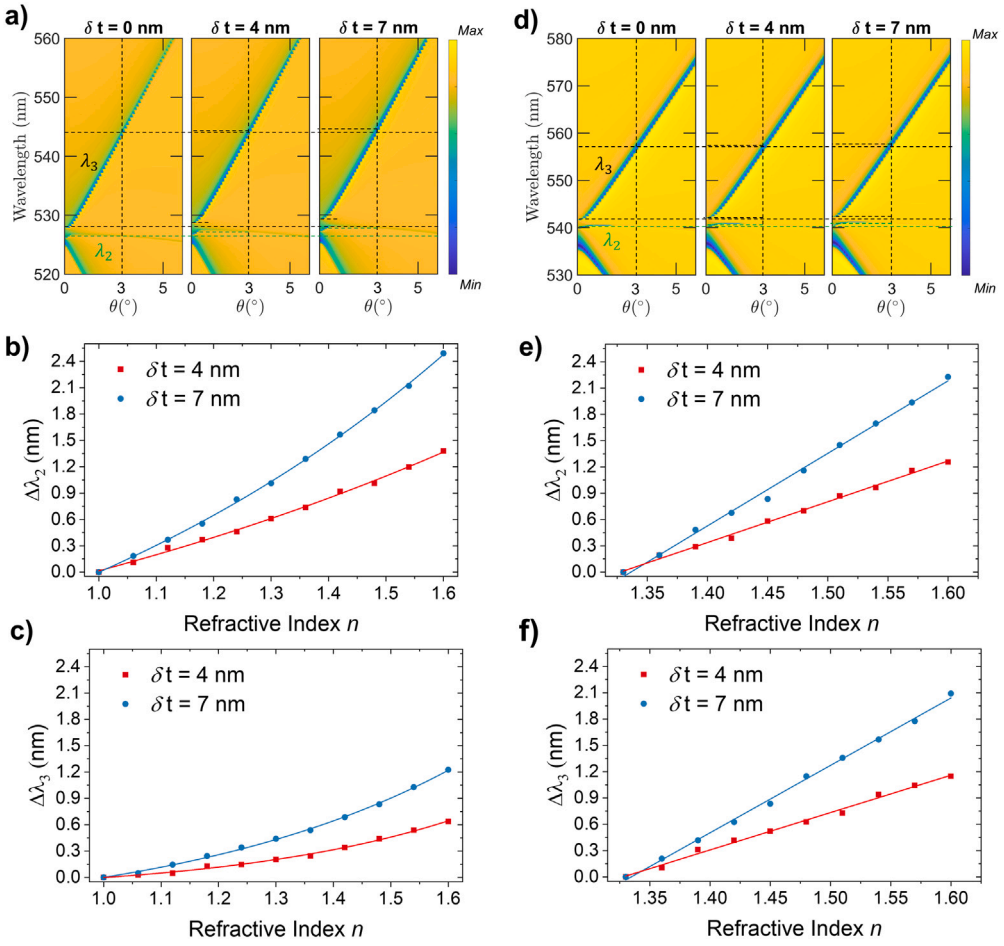

Fig. 2. (a) Simulated transmittance (s-pol) band diagrams of a PhCS (r = 95 nm, t = 56 nm, and a = 363 nm) in air (cladding refractive index $n_{cladding}$ = 1.0) with a biorecognition layer with refractive index of 1.42 and thickness δt = 0, 4, 7 nm. Theoretical wavelength shifts $\Delta\lambda(3°)$ of modes (b) λ_2 and (c) λ_3 as a function of the bio-film with increasing refractive index (from 1.0 to 1.6) with δt = 4 nm (red) and 7 nm (blue) with $n_{cladding}$ = 1.0. (d) Simulated transmittance (s-pol) band diagrams of a PhCS (r = 95 nm, t = 56 nm, and a = 363 nm) in buffer (cladding refractive index = 1.33) with a biorecognition layer with refractive index of 1.42 and thickness δt = 0, 4, 7 nm. Theoretical wavelength shifts $\Delta\lambda(3°)$ of modes (e) λ_2 and (f) λ_3 as a function of the bio-film with increasing refractive index (from 1.33 to 1.60) with δt = 4 nm (red) and 7 nm (blue) with $n_{cladding}$ = 1.33.

3.3. Optimization of the functionalization protocol

The evaluation of the dissociation constant required optimizing the functionalization strategy to achieve a reversible interaction between the two proteins. Two sets of PhCSs were prepared, one with SPARC as a bioprobe and the other with HSA as a bioprobe. The immobilization of the bioprobes followed the same preparation steps (Fig. 3a): piranha treatment, silanization with APTES, and BS^3 crosslinking. The crosslinking step was followed by incubation with SPARC (14 μM) on one set and HSA (7 μM) on the other. Covalent immobilization of the bioprobe was followed by a passivation step in the TRIS-HCl buffer to block the high reactivity of the BS^3 crosslinker. To test the efficiency of interaction reversibility, HSA (0.3 nM) and SPARC (1.0 nM) solutions in PBS (pH 7.4) were drop-cast on SPARC-functionalized PhCSs and HSA-functionalized PhCSs, respectively. The dissociation of the analyte from its bioprobe was induced by a pH variation, achieved by incubating the samples in a HEPES buffer solution at pH 5.0. After each incubation step, band diagrams were acquired as described in the Experimental Section (Fig. 3b–d). The variation of the third mode λ_3 with a BIC in the Γ point as a function of the functionalization step was monitored for both strategies. The peak shift $\Delta\lambda$ between the current functionalization step and the pristine PhCS samples was reported as mean ± standard deviation (SD).

In Fig. 3c, the evolution of $\Delta\lambda$ due to SPARC immobilization and HSA recognition is shown. A $\Delta\lambda \approx 2.45 \pm 0.12$ nm shift was obtained after silanization, with a further 0.4 nm redshift ($\Delta\lambda \approx 2.85 \pm 0.12$ nm) observed following interaction with SPARC. The passivation step with TRIS-HCl did not cause any significant change in the resonance position. Finally, interaction with HSA resulted in an additional redshift of λ_3 by 0.3 nm ($\Delta\lambda \approx 3.15 \pm 0.13$ nm), which remained stable after the washing step with HEPES.

The histogram in Fig. 3e shows $\Delta\lambda$ obtained using HSA as a bioprobe and SPARC as a target molecule. Specifically, $\Delta\lambda \approx 2.45 \pm 0.12$ nm after silanization, and $\Delta\lambda \approx 2.97 \pm 0.12$ nm following interaction with HSA. The higher value is attributed to the greater molecular weight of HSA compared to the SPARC protein, which affects the effective refractive index on the PhCS surface. The passivation step with TRIS-HCl did not cause any significant change in the resonance position. Finally, interaction with SPARC produced an additional 0.3 nm-redshift ($\Delta\lambda \approx 3.35 \pm 0.13$ nm). The washing step in HEPES resulted this time in a blue shift of 0.3 nm, denoting significant removal of the SPARC protein without affecting the HSA bioprobe. This suggested the possibility of regenerating the sensor with the HEPES buffer between one analyte concentration and the subsequent one in continuous monitoring experiments. The results emphasize the reversible nature of the binding of SPARC to HSA while confirming the nonspecific interactions of HSA on the SPARC-functionalized PhCS (see also Figure S6 from the Supporting Information). This highlights the importance of carefully selecting which protein to immobilize for optimal assay performance, especially for continuous monitoring applications. HSA and, in general, albumins are known for their strong surface adherence, as they are commonly used as passivation agents to reduce nonspecific binding in

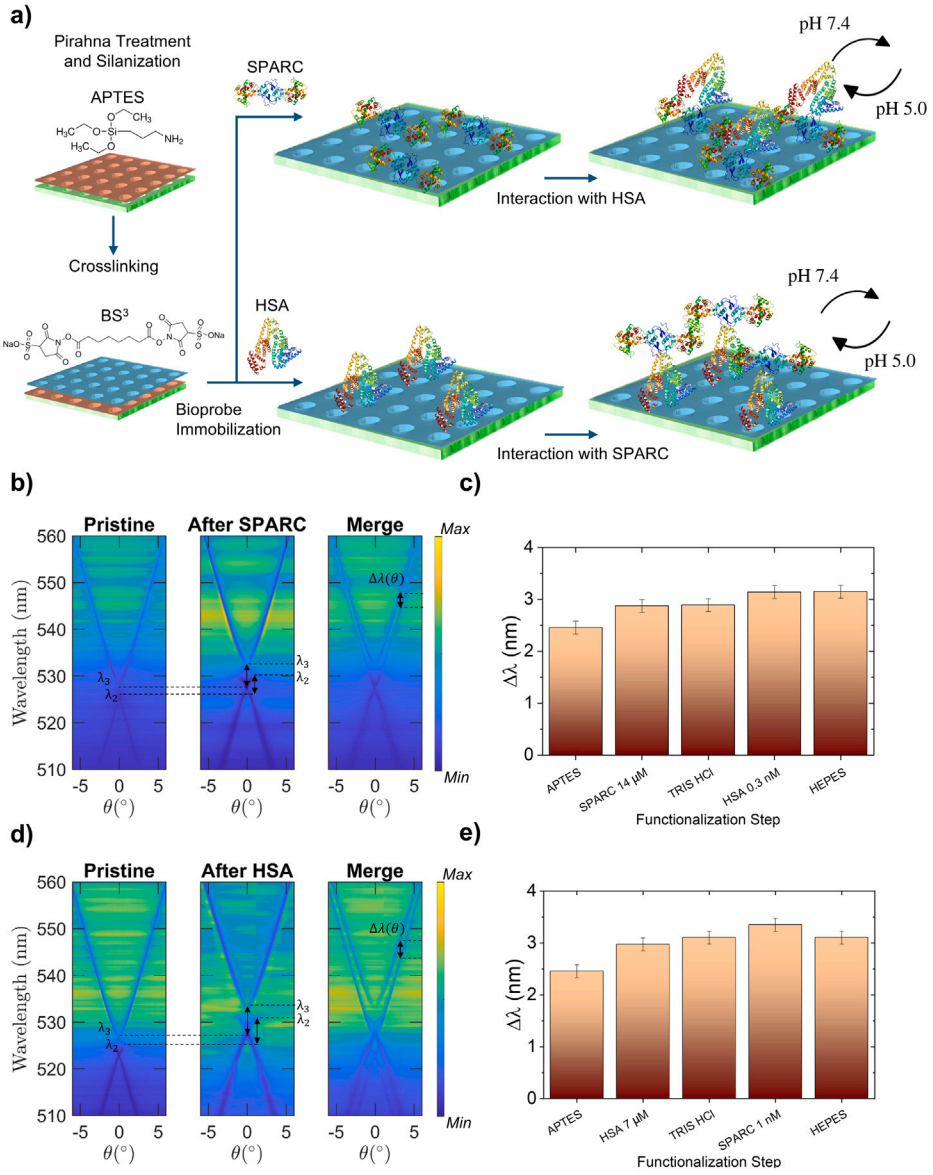

Fig. 3. (a) Schematic representation of the adopted functionalization strategies. (b) Comparison of the transmittance bands before (pristine) and after incubation with SPARC (concentration C = 14 μM), and normalized difference band diagram indicated as merge. (c) Histogram of the $\Delta\lambda(\theta)$ of the third mode λ_3 as a function of the functionalization step with SPARC as a bioprobe (14 μM) for $\theta \in (2°, 4°)$. (d) Comparison of the transmittance bands before (pristine) and after incubation with HSA (concentration C = 7 μM), and normalized difference band diagram indicated as merge. (e) Histogram of the $\Delta\lambda(\theta)$ of the third mode λ_3 as a function of the functionalization step with HSA as a bioprobe (7 μM) for $\theta \in (2°, 4°)$.

biosensing applications (Mulvihill et al., 1990; Keogh and Eaton, 1994). Immobilizing HSA rather than SPARC provides a more controlled and stable interface, minimizing background interference and enhancing the specificity of SPARC detection. In contrast, immobilizing SPARC leads to unpredictable interactions with HSA, which compromises the reliability of the assay. Furthermore, the natural role of HSA in binding and transporting biomolecules makes it a favorable substrate for immobilization, as it can maintain its functional integrity while providing a suitable environment for capturing SPARC. This strategic approach not only improves sensitivity but also ensures greater reproducibility.

3.4. Evaluation of the dissociation constant

The reaction between the immobilized ligand (HSA) and the analyte (SPARC) follows a pseudo-first-order kinetics. During the association phase, the complex [HSA-SPARC] increases as a function of time according to the following kinetic equation:

$$\frac{d[\text{HSA-SPARC}]}{dt} = k_a[\text{HSA}][\text{SPARC}] - k_d[\text{HSA-SPARC}] \quad (1)$$

The association rate constant k_a describes the rate of complex formation, *i.e.* the number of HSA-SPARC complexes formed per second in 1 M solution of HSA and SPARC ($k_a = [\text{M}^{-1}\text{s}^{-1}]$). The dissociation rate constant k_d describes the stability of the complex, *i.e.* the fraction of complexes that decays per second ($k_d = [\text{s}^{-1}]$).

The kinetic equation can be transformed into a so-called integrated rate equation, which can be used to fit the experimental data:

$$R = R_{eq}(1 - e^{-(k_a \cdot C_{\text{SPARC}} + k_d)(t - t_0)}) \quad (2)$$

where R and R_{eq} are the physical readout parameters defining the binding transduction over time in the sensor, e.g. the shift of Fano peak of the resonance tracked over time $\Delta\lambda(t)$ and its equilibrium condition $\Delta\lambda_{eq}$, respectively.

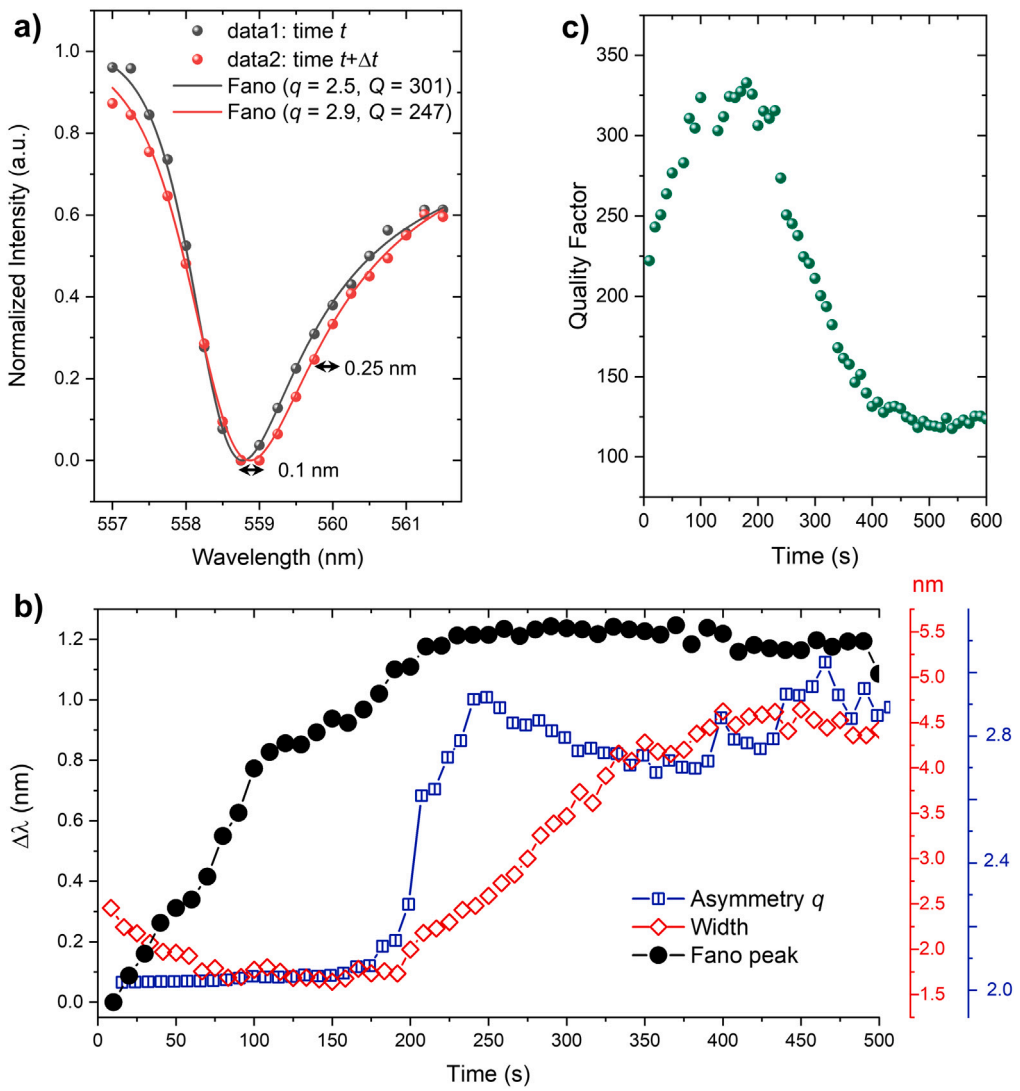

Fig. 4. (a) Example of Fano-shaped peak evolution upon binding: Fano asymmetry and quality factor change with the spectral shape, so that the tracking parameter η, *i.e.*, the spectral position of derivative maximum, shifts more than the peak position, 0.25 nm vs. 0.1 nm in this case. (b) Typical evolution over time of the resonance spectral profile upon analyte binding. (c) Related evolution of the quality factor, with its characteristic drop upon molecular binding.

When the analyte flowing over the sensor surface is replaced by the buffer solution, its free concentration rapidly drops to zero, initiating the dissociation of the complex. By neglecting the rebinding of the released analyte, dissociation can be described by the rate equation:

$$\frac{dR}{dt} = -k_d \cdot R \tag{3}$$

The dissociation rate constant (k_d) can be reliably measured by dissociating the analyte from the ligand after the buffer replaces the analyte solution. Also in this case, it is possible to fit the integrated rate equation to the experimental data:

$$R = R_0 \cdot e^{-k_d(t-t_0)} + R_{(t\to\infty)} \tag{4}$$

where $R_0 = \Delta\lambda(t = 0s)$ and $R_{(t\to\infty)}$ is the offset to be considered when at $t \to \infty$ the sensogram has not returned to zero.

Fig. 4a presents the typical redshift of the Fano resonance peak upon molecular binding in the transmittance spectrum. The profile can be fitted to

$$I(\lambda)/I_0 = 1 - \frac{(q + 2(\lambda - \lambda_0)/\sigma)^2}{1 + 4(\lambda - \lambda_0)^2/\sigma^2}, \tag{5}$$

with peak λ_0, linewidth σ and asymmetry parameter q. Instead of relying solely on peak shifts, we analyzed the full spectral evolution, tracking variations in σ and q over time, and hence the quality factor. Typically, Q decreases upon molecular binding (Zito et al., 2024). This approach enabled the definition of a more sensitive readout parameter, the tracking parameter η, which monitors the maximum derivative position. Since resonance broadening amplifies η variations, it provides enhanced sensitivity. In the example shown, η shifts by 0.25 nm, compared to a peak shift of only 0.1 nm. Fig. 4b illustrates the evolution of the Fano profile over time following the release analyte at $t = 0$. Fig. 4c shows the corresponding evolution of the resonance quality factor: after an initial increase, once binding stabilizes, resonator losses increase. By combining these metrics, we achieved accurate quantification of binding kinetics while mitigating alignment or other possible instabilities over extended acquisitions (30–60 min).

Eqs. (2)–(4) were employed to fit the experimental data and extract the association and dissociation rate constants of SPARC binding to HSA. Fig. 5a presents the experimental band diagrams of the HSA-functionalized photonic crystal slab (PhCS) inside the microfluidic chamber, recorded both before and after incubation with SPARC at a concentration of 1 nM. As predicted by numerical simulations, the bound state in the continuum (BIC)-associated mode λ_3 exhibits a significant red shift of approximately 14 nm upon immersion in PBS, attributed to the high bulk sensitivity of the PhCS. Following incubation

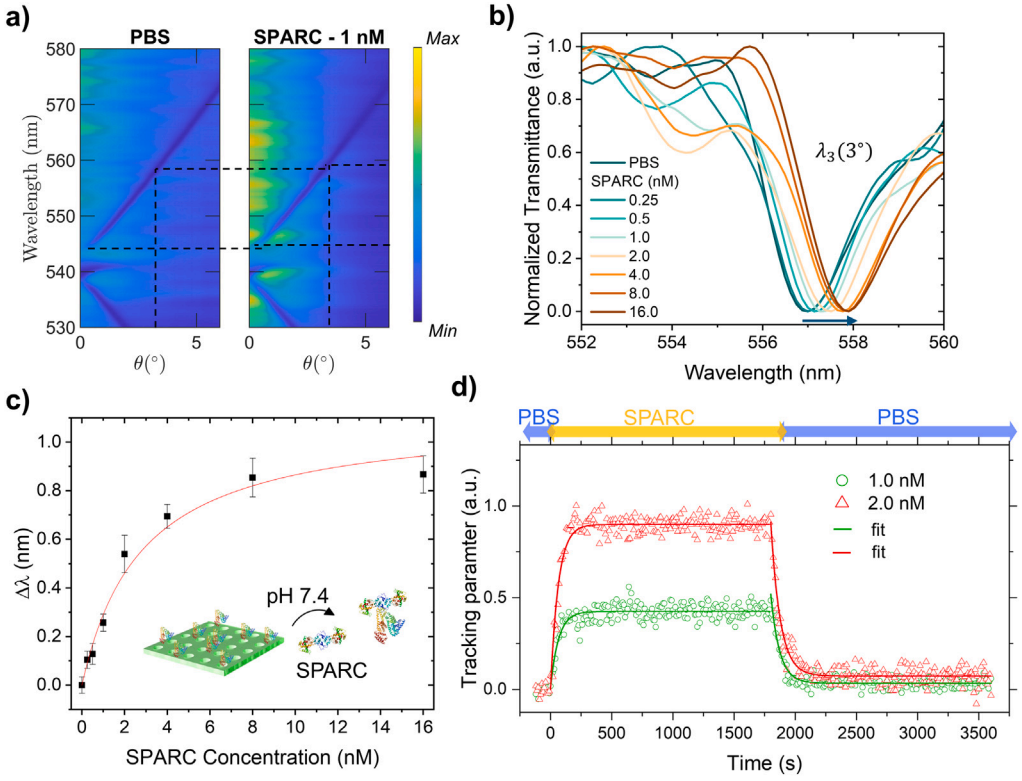

Fig. 5. (a) Transmittance bands before (PBS) and after incubation with SPARC (C = 1 nM). (b) Normalized transmittance spectra of the third mode λ_3 as a function of the SPARC concentration after the equilibrium (PBS, 0.25, 0.5, 1.0, 2.0, 4.0, 8.0, and 16.0 nM) at $\theta = 3°$. (c) Mean $\Delta\lambda$ (over the incidence angle θ) of λ_3 after incubation with SPARC at different concentrations (0.25, 0.5, 1.0, 2.0, 4.0, 8.0, and 16.0 nM). Curve fitting was performed using the Michaelis Menten equation. The reaction has been carried out at pH 7.4 in PBS buffer. Vertical bars denote the SD obtained for an incidence angle range spanning from ±2° to ±4° with a step of 0.01°. (d) Sensorgram showing the evolution of the tracking parameter after incubation with SPARC protein at 1.0 nM (green), and 2.0 nM (red). Before each SPARC incubation (indicated with yellow arrow), the HSA-functionalized PhCS was initialized in PBS (pH 7.4 - blue arrow). The dissociation phase was carried out after SPARC association in the same buffer (PBS pH 7.4 - blue arrow). The association kinetics fitting curves were obtained by using Eq. (2). The dissociation kinetics fitting curves were obtained by using Eq. (4).

with SPARC, a further red shift is observed — up to 0.8 nm at a SPARC concentration of 16 nM — which strongly suggests that molecular interactions are occurring at the functionalized surface.

To quantify the interaction dynamics, the response of λ_3 was monitored across a range of SPARC concentrations. As shown in Fig. 5b, the wavelength shift follows a concentration-dependent trend, progressively increasing with higher SPARC concentrations until reaching saturation at 8 nM. This plateau suggests that all available binding sites on the HSA-functionalized surface are occupied at this concentration, indicating the establishment of equilibrium.

The association phase was conducted at a constant flow rate of 10 μL/min to ensure accurate kinetic measurements and minimize mass transport limitations. After each association step, band diagrams were recorded to track the real-time binding events. These data were further analyzed to construct the dose–response curve shown in Fig. 5c, which depicts the dependence of the wavelength shift ($\Delta\lambda$) on SPARC concentration. The shift was measured statistically, averaging λ_3 in the angular range $\theta \in (2°, 4°)$, ensuring high precision in the detection process (see also Figure S7). Blank measurements (PBS 1x, pH 7.4) confirmed no significant shifts during incubation, as shown in Fig. 5c.

The fitting of the dose–response curve was performed using a Michaelis–Menten model, a well-established approach for characterizing biomolecular interactions. This analysis confirmed a 1:1 binding stoichiometry between HSA and SPARC, reinforcing the specificity of the interaction. The derived binding parameters provide valuable insights into the kinetic and thermodynamic properties of SPARC-HSA interactions, with potential implications for biomolecular sensing applications.

In this experimental context, the limit of detection (LOD) was not considered a critical parameter, as the focus was not on detecting trace concentrations in complex samples, but rather on ensuring signal stability and enabling accurate, real-time monitoring of binding kinetics.

Finally, Fig. 5d presents the sensograms depicting the real-time evolution of tracking parameter $\eta(\lambda_3)$ at an incident angle of $\theta \approx 0.5°$, recorded for SPARC concentrations 1.0 and 2.0 nM. To ensure a well-defined baseline, the sensor was first equilibrated in PBS buffer for 60 s before introducing the SPARC solution into the microfluidic channel using a syringe pump. The temporal evolution of the wavelength shift was then continuously monitored to capture the association kinetics of SPARC binding to the HSA-functionalized PhCS. Once the signal stabilized, indicating that equilibrium had been reached, the solution containing SPARC molecules was replaced with its corresponding buffer, allowing us to track the dissociation phase. The progressive decrease in wavelength shift confirmed the detachment of SPARC molecules from the sensor surface, and measurements continued until the signal reached a stable baseline. To ensure reproducibility and eliminate residual bound molecules, the sensor surface was regenerated using HEPES buffer, after which the experiment was repeated with progressively higher SPARC concentrations. A maximum of 2–3 regeneration cycles was performed, as beyond this number a gradual degradation in sensor response was observed.

The experimental data were analyzed by fitting the sensogram curves using Eqs. (2)–(4), and the extracted kinetic parameters are summarized in Table 1. By averaging the results across the three tested SPARC concentrations, we determined an association rate constant of $k_a = (1.7 \pm 0.2) \times 10^6$ $M^{-1}s^{-1}$ and a dissociation rate constant of $k_d = (1.4 \pm 0.1) \times 10^{-2}$ s^{-1}. From these values, the equilibrium dissociation constant was calculated using the relationship $K_D = k_d/k_a$, yielding a final value of $K_D = 8.2 \pm 0.8$ nM.

Table 1
Kinetic parameters for SPARC binding at different concentrations.

SPARC C (nM)	k_a ($s^{-1}M^{-1}$)	k_d (s^{-1})	K_D (nM)
1.0	1.8×10^6	1.4×10^{-2}	7.71
2.0	1.5×10^6	1.3×10^{-2}	8.82
Average	$1.7 \pm 0.2 \times 10^6$	$1.4 \pm 0.1 \times 10^{-2}$	8.2 ± 0.8

This is particularly relevant considering the significant variability in K_D values for the SPARC-HSA interaction poorly reported in the literature, which ranges from as low as 1 nM to as high as 100 μM. However, while specific values for the SPARC-HSA complex dissociation constant are poorly available, several studies have demonstrated a significant binding affinity between these two proteins (Park et al., 2019; Knauer et al., 2009; Merlot et al., 2014; Zheng et al., 2024). These studies confirm a meaningful binding affinity between SPARC and HSA and highlight the need for more quantitative studies to determine the exact dissociation constant for this interaction.

Our results are in good agreement with the recently reported value for the case of HSA immobilized on the substrate (Cini et al., 2023). The obtained kinetic and equilibrium parameters provide a quantitative assessment of the affinity between SPARC and HSA, further validating the specificity and robustness of the PhCS-based biosensing approach.

4. Conclusions

In this work, we develop and validate a BIC-based optical biosensor for real-time monitoring of high-affinity protein–protein interaction. We apply the BIC-biosensor to the challenging study of SPARC-HSA interaction, accurately resolving their fast kinetics with our label-free ultrasensitive detection. By leveraging the high Q-factor of BICs, we achieve precise determination of the kinetic parameters at sub-nanomolar concentration range. This unravels an association rate constant $k_a = (1.7 \pm 0.2) \times 10^6$ $M^{-1}s^{-1}$ and a dissociation rate constant $k_d = (1.4 \pm 0.1) \times 10^{-2}$ s^{-1}, leading to a dissociation constant $K_D = 8.2 \pm 0.8$ nM. These results confirm a strong binding affinity between SPARC and HSA, which reinforces the role of this interaction in tumor biology and its potential implications for drug delivery strategies. Compared to standard techniques such as SPR and ELISA, the BIC-based device demonstrates superior performance in terms of sensitivity, reduced optical losses, and a simplified, label-free detection protocol. In direct experimental comparison, the dissociation constant (K_D) obtained via SPR was 18.9 ± 2.3 μM (Chlenski et al., 2016), whereas the BIC-based platform yielded significantly lower values. This difference is attributable to the alternative immobilization strategy employed, which minimizes nonspecific interactions and enhances detection specificity for SPARC. Differently, ELISA assays reported K_D values on the order of ≈10 nM (Cini et al., 2023), values comparable to those of the proposed BIC-based platform. However, such assays rely on antibodies and conjugated fluorophores or enzymes, which are not cost-effective and introduce additional complexity. The BIC-based method achieves equivalent or superior affinity measurements without the need for antibodies or labeling, representing a robust and scalable approach for high-specificity, cost-effective biosensing.

These attributes make it particularly suited for detecting biomolecular interactions at low analyte concentrations, a critical requirement for biomedical applications. Additionally, the scalability and compact design of the platform pave the way for its integration into portable diagnostic devices, offering new opportunities for point-of-care applications in cancer diagnostics and therapeutic monitoring. By providing a robust and highly sensitive method for studying SPARC-HSA interactions, this work contributes to a deeper understanding of their role in tumor microenvironments and targeted drug delivery systems. Future developments will focus on expanding the capabilities of the proposed platform to multiplexed detection and its potential clinical translation for precision medicine applications.

CRediT authorship contribution statement

Bruno Miranda: Writing – review & editing, Writing – original draft, Software, Methodology, Investigation, Formal analysis, Data curation. **Vincenza Mele:** Writing – original draft, Methodology, Investigation. **Aida Seifalinezhad:** Writing – original draft, Investigation. **Gianluigi Zito:** Writing – review & editing, Validation, Software, Methodology, Investigation, Funding acquisition, Formal analysis, Data curation, Conceptualization. **Adam Schwartzberg:** Resources, Methodology. **Vito Mocella:** Writing – review & editing, Visualization, Supervision, Resources, Funding acquisition. **Ivo Rendina:** Resources, Funding acquisition. **Annalisa Lamberti:** Writing – review & editing, Supervision, Project administration, Methodology, Conceptualization. **Gennaro Sanità:** Writing – review & editing, Writing – original draft, Methodology, Investigation, Formal analysis. **Silvia Romano:** Writing – review & editing, Writing – original draft, Supervision, Project administration, Methodology, Investigation, Formal analysis, Data curation, Conceptualization.

Declaration of competing interest

The authors declare that they have no known competing financial interests or personal relationships that could have appeared to influence the work reported in this paper.

Acknowledgments

We are thankful to Scott Dhuey, Molecular Foundry, Lawrence Berkeley National Laboratory, USA, for assistance in the fabrication process and Mariorosario Masullo, University of Naples "Parthenope" for fruitful discussions. V.M. and B. M. acknowledge the EU Italian National Recovery and Resilience Plan (NRRP) of NextGenerationEU (PE0000023-NQSTI). I.R., A. L. and S. R. acknowledge financial support by PRIN Project BPLAS, grant no. 2022TXWE32 Italian Ministry of University and Research (MUR), Italy. G. S. acknowledges the EU Italian National Recovery and Resilience Plan (NRRP) of NextGenerationEU (PE00000001-RESTART). G.Z. acknowledges financial support from the European Union – NextGenerationEU, under the National Recovery and Resilience Plan (NRRP), Mission 4, Component C2 Investment 1.1, PRIN project INSPIRE, grant no. P2022LETN5. Work at the Molecular Foundry was supported by the Office of Science, Office of Basic Energy Sciences, of the U.S. Department of Energy under Contract No. DE-AC02-05CH11231.

Appendix A. Supplementary data

Supplementary material related to this article can be found online at https://doi.org/10.1016/j.bios.2025.117754.

Data availability

Data will be made available on request.

References

Tai, I.T., Tang, M.J., 2008. SPARC in cancer biology: its role in cancer progression and potential for therapy. Drug Resist. Updat. 11 (6), 231–246.
Johnson, A., Smith, R., 2002. SPARC: A matrix protein with important implications for cancer. Cancer Res. 62 (3), 156–162.
Liu, M., Zeng, F., 2014. SPARC and tumor microenvironment interactions. J. Cell. Biol. 207 (2), 231–239.
Andriani, F., Landoni, E., Mensah, M., Facchinetti, F., Miceli, R., Tagliabue, E., Giussani, M., Callari, M., De Cecco, L., Colombo, M.P., et al., 2018. Diagnostic role of circulating extracellular matrix-related proteins in non-small cell lung cancer. BMC Cancer 18, 1–14.
Ghanemi, A., Yoshioka, M., St-Amand, J., 2020. Secreted protein acidic and rich in cysteine and cancer: A homeostatic hormone? Cytokine 127, 154996.

Vishnu, P., Roy, V., 2011. Safety and efficacy of nab-paclitaxel in the treatment of patients with breast cancer. Breast Cancer: Basic Clin. Res. 5, BCBCR–S5857.
Carrese, B., Cavallini, C., Sanità, G., Armanetti, P., Silvestri, B., Calì, G., Pota, G., Luciani, G., Menichetti, L., Lamberti, A., 2021. Controlled release of doxorubicin for targeted chemo-photothermal therapy in breast cancer HS578t cells using albumin modified hybrid nanocarriers. Int. J. Mol. Sci. 22 (20), 11228.
Carrese, B., Cavallini, C., Armanetti, P., Silvestri, B., Calì, G., Luciani, G., Sanità, G., Menichetti, L., Lamberti, A., 2023. Hybrid nanoparticle-assisted chemo-photothermal therapy and photoacoustic imaging in a three-dimensional breast cancer cell model. Int. J. Mol. Sci. 24 (24), 17374.
Zhao, P., Wang, Y., Wu, A., Rao, Y., Huang, Y., 2018. Roles of albumin-binding proteins in cancer progression and biomimetic targeted drug delivery. ChemBioChem 19 (17), 1796–1805.
Belinskaia, D., Voronina, P., Goncharov, N., 2021. Integrative role of albumin: evolutionary, biochemical and pathophysiological aspects. J. Evol. Biochem. Physiol. 57, 1419–1448.
Chlenski, A., Dobratic, M., Salwen, H.R., Applebaum, M., Guerrero, L.J., Miller, R., DeWane, G., Solomaha, E., Marks, J.D., Cohn, S.L., 2016. Secreted protein acidic and rich in cysteine (SPARC) induces lipotoxicity in neuroblastoma by regulating transport of albumin complexed with fatty acids. Oncotarget 7 (47), 77696.
Ji, Q., Zhu, H., Qin, Y., Zhang, R., Wang, L., Zhang, E., Zhou, X., Meng, R., 2024. GP60 and SPARC as albumin receptors: key targeted sites for the delivery of antitumor drugs. Front. Pharmacol. 15, 1329636.
Aarons, L., 1981. Kinetics of drug-drug interactions. Pharmacol. Ther. 14 (3), 321–344. http://dx.doi.org/10.1016/0163-7258(81)90031-0.
Giannetti, A.M., Koch, B.D., Browner, M.F., 2008. Surface plasmon resonance based assay for the detection and characterization of promiscuous inhibitors. J. Med. Chem. 51 (3), 574–580. http://dx.doi.org/10.1021/jm700952v, arXiv:https://doi.org/10.1021/jm700952v. PMID: 18181566.
Copeland, R.A., 2016. The drug–target residence time model: a 10-year retrospective. Nat. Rev. Drug Discov. 15 (2), 87–95.
Bulgakov, E.N., Sadreev, A.F., 2008. Bound states in the continuum in photonic waveguides inspired by defects. Phys. Rev. B Condens. Matter Mater. Phys. 78, 0751051.
Plotnik, Y., Peleg, O., Dreisow, F., Heinrich, M., Nolte, S., Szameit, A., Segev, M., 2011. Experimental observation of optical bound states in the continuum. Phys. Rev. Lett. 107 (18), 183901.
Molina, M.I., Miroshnichenko, A.E., Kivshar, Y.S., 2012. Surface bound states in the continuum. Phys. Rev. Lett. 108 (7), 070401.
Hsu, C.W., Zhen, B., Lee, J., Chua, S.-L., Johnson, S.G., Joannopoulos, J.D., Soljačić, M., 2013b. Observation of trapped light within the radiation continuum. Nature 499 (7457), 188–191.
Zhen, B., Hsu, C.W., Lu, L., Stone, A.D., Soljačić, M., 2014. Topological nature of optical bound states in the continuum. Phys. Rev. Lett. 113 (25), 257401.
Bulgakov, E.N., Sadreev, A.F., 2014. Bloch bound states in the radiation continuum in a periodic array of dielectric rods. Phys. Rev. A 90 (5), 053801.
Mocella, V., Romano, S., 2015. Giant field enhancement in photonic resonant lattices. Phys. Rev. B 92 (15), 155117.
Gomis-Bresco, J., Artigas, D., Torner, L., 2017. Anisotropy-induced photonic bound states in the continuum. Nat. Photonics 11 (4), 232–236.
von Neumann, J., Wigner, E.P., 1929. Über merkwürdige diskrete Eigenwerte. Phys. Z. 30, 465–467.
Gansch, R., Kalchmair, S., Genevet, P., Zederbauer, T., Detz, H., Andrews, A.M., Schrenk, W., Capasso, F., Lončar, M., Strasser, G., 2016. Measurement of bound states in the continuum by a detector embedded in a photonic crystal. Light. Sci. Appl. 5 (9), e16147–e16147.
Bulgakov, E.N., Maksimov, D.N., 2018. Optical response induced by bound states in the continuum in arrays of dielectric spheres. J. Opt. Soc. Am. B 35 (10), 2443–2452. http://dx.doi.org/10.1364/josab.35.002443.
Kupriianov, A.S., Xu, Y., Sayanskiy, A., Dmitriev, V., Kivshar, Y.S., Tuz, V.R., 2019. Metasurface engineering through bound states in the continuum. Phys. Rev. Appl. 12 (1), 014024.
Gao, X., Zhen, B., Soljacic, M., Chen, H., Hsu, C.W., 2019. Bound states in the continuum in fiber bragg gratings. ACS Photonics 6 (11), 2996–3002.
Hsu, C.W., Zhen, B., Lee, J., Chua, S.-l., Johnson, S.G., Joannopoulos, J.D., Soljac, M., 2013a. Observation of trapped light within the. Nature 499, 188–191. http://dx.doi.org/10.1038/nature12289.
Ma, X., Ma, Y., Cunha, P., Liu, Q., Kudtarkar, K., Xu, D., Wang, J., Chen, Y., Wong, Z.J., Liu, M., et al., 2022. Strategical deep learning for photonic bound states in the continuum. Laser Photonics Rev. 16 (10), 2100658.
Chen, Y., Yu, J., Zhang, W., Huang, W., 2024. Inverse design of quasi-bound states in the continuum absorber. IEEE J. Quantum Electron..
Zito, G., Romano, S., Cabrini, S., Calafiore, G., De Luca, A.C., Penzo, E., Mocella, V., 2019. Observation of spin-polarized directive coupling of light at bound states in the continuum. Optica 6 (10), 1305–1312.
Wang, B., Liu, W., Zhao, M., Wang, J., Zhang, Y., Chen, A., Guan, F., Liu, X., Shi, L., Zi, J., 2020. Generating optical vortex beams by momentum-space polarization vortices centred at bound states in the continuum. Nat. Photonics 14 (10), 623–628.
Cerjan, A., Jürgensen, M., Benalcazar, W.A., Mukherjee, S., Rechtsman, M.C., 2020. Observation of a higher-order topological bound state in the continuum. Phys. Rev. Lett. 125 (21), 213901.
De Tommasi, E., Esposito, E., Romano, S., Crescitelli, A., Di Meo, V., Mocella, V., Zito, G., Rendina, I., 2021. Frontiers of light manipulation in natural, metallic, and dielectric nanostructures. Riv. Nuovo Cimento 1–68.
De Tommasi, E., Romano, S., Mocella, V., Sgrignuoli, F., Lanzio, V., Cabrini, S., Zito, G., 2023. Half-integer topological charge polarization of quasi-Dirac bound states in the continuum. Adv. Opt. Mater. 2300475.
Schiattarella, C., Romano, S., Sirleto, L., Mocella, V., Rendina, I., Lanzio, V., Riminucci, F., Schwartzberg, A., Cabrini, S., Chen, J., et al., 2024. Directive giant upconversion by supercritical bound states in the continuum. Nature 626 (8000), 765–771.
Hwang, M.-S., Lee, H.-C., Kim, K.-H., Jeong, K.-Y., Kwon, S.-H., Koshelev, K., Kivshar, Y., Park, H.-G., 2021. Ultralow-threshold laser using super-bound states in the continuum. Nat. Commun. 12 (1), 1–9.
Yu, Y., Sakanas, A., Zali, A.R., Semenova, E., Yvind, K., Mørk, J., 2021. Ultra-coherent Fano laser based on a bound state in the continuum. Nat. Photonics 15 (10), 758–764.
Do, T.T.H., Yuan, Z., Durmusoglu, E.G., Shamkhi, H.K., Valuckas, V., Zhao, C., Kuznetsov, A.I., Demir, H.V., Dang, C., Nguyen, H.S., et al., 2025. Room-temperature lasing at flatband bound states in the continuum. ACS Nano.
Foley, J.M., Young, S.M., Phillips, J.D., 2014. Symmetry-protected mode coupling near normal incidence for narrow-band transmission filtering in a dielectric grating. Phys. Rev. B 89 (16), 165111.
Lu, Q., Feng, Z., Sun, X., 2024. Symmetry-protected bound states in the continuum on an integrated photonic platform. Nanophotonics 13 (18), 3527–3534.
Liu, Y., Zhou, W., Sun, Y., 2017. Optical refractive index sensing based on high-q bound states in the continuum in free-space coupled photonic crystal slabs. Sensors 17 (8), 1861.
Romano, S., Zito, G., Torino, S., Cabrini, S., Rendina, I., Coppola, G., Calafiore, G., Penzo, E., Mocella, V., 2018b. Label-free sensing of ultralow-weight molecules with all-dielectric metasurfaces supporting bound states in the continuum. Photonics Res. 6 (7), 726–733.
Romano, S., Lamberti, A., Masullo, M., Penzo, E., Cabrini, S., Rendina, I., Mocella, V., 2018a. Optical biosensors based on photonic crystals supporting bound states in the continuum. Materials 11 (4), 1–11. http://dx.doi.org/10.3390/ma11040526.
Romano, S., Zito, G., Yépez, S.N.L., Cabrini, S., Penzo, E., Coppola, G., Rendina, I., Mocella, V., 2019. Tuning the exponential sensitivity of a bound-state-in-continuum optical sensor. Opt. Express 27 (13), 18776–18786.
Yesilkoy, F., Arvelo, E.R., Jahani, Y., Liu, M., Tittl, A., Cevher, V., Kivshar, Y., Altug, H., 2019. Ultrasensitive hyperspectral imaging and biodetection enabled by dielectric metasurfaces. Nat. Photonics 13 (6), 390–396.
Romano, S., Mangini, M., Penzo, E., Cabrini, S., De Luca, A.C., Rendina, I., Mocella, V., Zito, G., 2020. Ultrasensitive surface refractive index imaging based on quasi-bound states in the continuum. ACS Nano 14 (11), 15417–15427.
Maksimov, D.N., Gerasimov, V.S., Romano, S., Polyutov, S.P., 2020. Refractive index sensing with optical bound states in the continuum. Opt. Express 28 (26), 38907–38916.
Zito, G., Sanità, G., Alulema, B.G., Yépez, S.N.L., Lanzio, V., Riminucci, F., Cabrini, S., Moccia, M., Avitabile, C., Lamberti, A., et al., 2021. Label-free DNA biosensing by topological light confinement. Nanophotonics 10 (17), 4279–4287.
Schiattarella, C., Sanità, G., Alulema, B.G., Lanzio, V., Cabrini, S., Lamberti, A., Rendina, I., Mocella, V., Zito, G., Romano, S., 2022. High-q photonic aptasensor based on avoided crossing bound states in the continuum and trace detection of ochratoxin a. Biosens. Bioelectron: X 12, 100262.
Zito, G., Siciliano, G., Seifalinezhad, A., Miranda, B., Lanzio, V., Schwartzberg, A., Gigli, G., Turco, A., Rendina, I., Mocella, V., et al., 2024. Molecularly imprinted polymer sensor empowered by bound states in the continuum for selective trace-detection of TGF-beta. Adv. Sci. 11 (41), 2401843.
Clabassi, E., Balestra, G., Siciliano, G., Polimeno, L., Tarantini, I., Primiceri, E., Tobaldi, D.M., Cuscunà, M., Quaranta, F., Passaseo, A., et al., 2025. Hybrid plasmonic symmetry-protected bound state in the continuum entering the zeptomolar biodetection range. Small 2411827.
Romano, S., Cabrini, S., Rendina, I., Mocella, V., 2014. Guided resonance in negative index photonic crystals: a new approach. Light.: Sci. Appl. 3 (1), e120–e120.
Guo, X., Tai, H., Li, X., Liu, P., Liu, J., Yu, S., 2024. SPARC is a novel prognostic biomarker for ovarian cancer and associated with immune signatures and drug response. Clin. Exp. Obs. Gynecol. 51 (3), 61.
Mulvihill, J.N., Faradji, A., Oberling, F., Cazenave, J.-P., 1990. Surface passivation by human albumin of plasmaperesis circuits reduces platelet accumulation and thrombus formation. Experimental and clinical studies. J. Biomed. Mater. Res. 24 (2), 155–163.
Keogh, J.R., Eaton, J.W., 1994. Albumin binding surfaces for biomaterials. J. Lab. Clin. Med. 124 (4), 537–545.
Park, C.R., Jo, J.H., Song, M.G., Park, J.Y., Kim, Y.-H., Youn, H., Paek, S.H., Chung, J.-K., Jeong, J.M., Lee, Y.-S., et al., 2019. Secreted protein acidic and rich in cysteine mediates active targeting of human serum albumin in U87MG xenograft mouse models. Theranostics 9 (24), 7447.

Knauer, D., Hwang, L., Lowe, C., Hwang, J., Norng, M., Trieu, V., Desai, N., 2009. Albumin-binding and angiogenic domains of SPARC located at its C-terminus. Cancer Res. 69 (24_Supplement), 2144–2144.

Merlot, A.M., Kalinowski, D.S., Richardson, D.R., 2014. Unraveling the mysteries of serum albumin—more than just a serum protein. Front. Physiol. 5, 299.

Zheng, B., Chen, Y., Niu, L., Zhang, X., Yang, Y., Wang, S., Chen, W., Cai, Z., Huang, W., Huang, W., 2024. Modulating the tumoral SPARC content to enhance albumin-based drug delivery for cancer therapy. J. Control. Release 366, 596–610.

Cini, J.K., Dexter, S., Rezac, D.J., McAndrew, S.J., Hedou, G., Brody, R., Eraslan, R.-N., Kenney, R.T., Mohan, P., 2023. SON-1210-a novel bifunctional IL-12/IL-15 fusion protein that improves cytokine half-life, targets tumors, and enhances therapeutic efficacy. Front. Immunol. 14, 1326927.